


Hall Thruster Performance and Efficiency Analysis of a Molecular Propellant

William P. Brabston,* Luke A. Marino,[†] Dan Lev,[‡] and Mitchell L. R. Walker[§]
Georgia Institute of Technology, Atlanta, Georgia 30332

<https://doi.org/10.2514/1.B39623>

An efficiency model is developed for Hall effect thrusters (HETs) operating on molecular propellants to inform which energy sinks lead to the largest degradations in HET efficiency. Similar to existing atomic efficiency models, the molecular model decomposes thrust efficiency into energy, propellant, and beam efficiencies and allows for the direct comparison of efficiencies between molecular and atomic propellants and between ionic species produced from a molecular propellant. The model was applied to experimental data on a 5 kW HET operating on nitrogen, argon, and xenon with a mass flow rate range of 5.0–5.4 mg/s and a discharge voltage range of 230–300 V. The measured thrust, specific impulse, and anode thrust efficiency ranges on each propellant are 72.8–86.8 mN, 1485–1770 s, and 32.9–39.6% (xenon); 90.2–111.9 mN, 1838–2280 s, and 25.2–29.0% (argon); and 61.4–90.0 mN, 1251–1724 s, and 12.8–16.9% (nitrogen), respectively. The low nitrogen efficiency is primarily attributed to poor mass utilization of atomic nitrogen ($\approx 27\%$) and decreased energy efficiency due to molecular-specific energy sinks, such as dissociation and excitation of molecular energy modes. Despite thrust efficiencies less than 17% at current power levels, nitrogen exhibits promise operating above 5 kW due to the high voltage utilization seen with the N^+ species ($\approx 89\%$).

Nomenclature

A_{en}	=	entrainment area, m^2	n_i	=	plasma density, m^{-3}
B	=	$E \times B$ applied magnetic field, G	P	=	chamber background pressure, Pa
\bar{c}_n	=	average thermal velocity of the n th species, m/s	P_d	=	discharge power, W
d	=	$E \times B$ plate separation distance, m	Q	=	average charge state of ionic particles
E	=	electric field strength, V/m	T	=	thrust, mN
E/N	=	reduced electric field, Td	T_{corr}	=	corrected thrust, mN
e	=	elementary charge, $1.602 \times 10^{-19} \text{C}$	T_e	=	electron temperature, eV
\mathcal{F}	=	Faraday constant, 96,485 C/mol	T_0	=	neutral temperature, K
f_e	=	normalized electron energy distribution function, eV^{-1}	V_a	=	atomic averaged acceleration voltage, V
I_{axial}	=	axial component of beam current, A	$V_{a,n}$	=	average acceleration voltage of the n th species, V
I_b	=	beam current, A	V_d	=	discharge voltage, V
$I_{b,\text{corr}}$	=	corrected beam current, A	V_p	=	plasma potential, V
$I_{b,n}$	=	beam current of the n th species, A	\bar{v}	=	average particle velocity, m/s
I_d	=	discharge current, A	$\frac{\bar{v}^2}{v^2}$	=	averaged particle squared velocity, m^2/s^2
$I_{d,\text{corr}}$	=	corrected discharge current, A	\bar{v}_i	=	average ion velocity, m/s
I_{sp}	=	specific impulse, s	$\bar{v}_{i,n}$	=	average ionic velocity of n th species, m/s
K_k	=	reaction rate constant of the k th reaction mechanism, m^3/s	\bar{v}_i^2	=	averaged ion squared velocity, m^2/s^2
k	=	Boltzmann constant, $1.38 \times 10^{-23} \text{m}^2 \cdot \text{kg}/\text{s}^2 \cdot \text{K}$	$\bar{v}_{0,n}$	=	average neutral velocity of n th species, m/s
\dot{m}_a	=	anode mass flow rate, mg/s	y_0	=	normalized neutral particle speed
\dot{m}_{en}	=	entrained background neutral mass flow rate, mg/s	Z_j	=	charge state of the j th charge species
\dot{m}_i	=	ion mass flow rate, mg/s	$\Delta V_{\text{plate},n}$	=	EXB plate voltage at n th species peak
$\dot{m}_{i,n}$	=	ionic mass flow rate of n th species, mg/s	$\frac{\partial n_k}{\partial t}$	=	k th mechanism reaction rate, $\text{m}^{-3} \cdot \text{s}^{-1}$
\mathcal{M}_n	=	molar mass of n th species, g/mol	ϵ_e	=	energy of impacted electron, eV
m_n	=	mass of n th particle, kg	ϵ_k	=	reaction energy of the k th reaction mechanism, eV
\dot{m}_n	=	mass flow rate of n th species, mg/s	ζ_A	=	area entrainment factor
N_n	=	n th species neutral number density, m^{-3}	ζ_{en}	=	thrust entrainment factor
			η_b	=	global current utilization
			$\eta_{b,n}$	=	species current utilization of n th species
			η_E	=	energy efficiency
			η_{SP}	=	species parameter efficiency
			η_T	=	anode thrust efficiency
			η_V	=	global voltage utilization
			$\eta_{V,n}$	=	species voltage utilization of n th species
			θ	=	plume angular location, $^\circ$
			θ_d	=	beam divergence angle, $^\circ$
			ξ_n	=	species fraction
			σ_k	=	cross section of the k th reaction mechanism, m^2
			Φ_m	=	mass utilization
			$\Phi_{m,n}$	=	species mass utilization
			Φ_{N-G}	=	neutral-gain utilization
			Φ_P	=	propellant efficiency
			Φ_q	=	charge utilization
			Φ_s	=	species utilization
			Ψ_b	=	beam efficiency

Received 14 May 2024; accepted for publication 23 May 2025; published online 22 August 2025. Copyright © 2025 by William Brabston, Luke Marino, Dan Lev, and Mitchell Walker. Published by the American Institute of Aeronautics and Astronautics, Inc., with permission. All requests for copying and permission to reprint should be submitted to CCC at www.copyright.com; employ the eISSN 1533-3876 to initiate your request. See also AIAA Rights and Permissions <https://aiaa.org/publications/publish-with-aiaa/rights-and-permissions/>.

*Graduate Student, Department of Aerospace Engineering; wbrabston3@gatech.edu.

[†]Graduate Student, Department of Aerospace Engineering; lukemario54@gatech.edu.

[‡]Research Engineer, Department of Aerospace Engineering; dan.lev@gatech.edu.

[§]Professor and Department Chair, Department of Aerospace Engineering; mitchell.walker@ae.gatech.edu.

$\Omega_{i,n}$	=	current fraction of n th species
Ω_j	=	current fraction of the j th charge species
$\langle \rangle_I$	=	current-averaged quantity
$\langle \rangle_m$	=	mass-averaged quantity
$\langle \rangle_{mv}$	=	momentum-averaged quantity

I. Introduction

MOLECULAR propellants have garnered interest for use in Hall effect thrusters (HETs). These propellants allow for HET-operated spacecraft to expand their potential mission profiles beyond that of more traditional atomic propellants, such as xenon and krypton [1]. Some prominent use cases of molecular propellants include multimode propulsion, using molecular propellants such as water and monopropellants, which could allow a satellite to operate in a high-thrust or high-efficiency mode while minimizing cost, weight, and complexity of the propulsion system [2–5]. Another use case is in-situ propulsion, using propellants such as air mixtures, which could allow satellites to operate in the currently restrictive very low Earth orbit (VLEO) by capturing atmospheric air in-situ and using this air as a propellant to compensate for the high VLEO drag force [6–10]. An additional use case is utilizing condensable and storable propellants, such as water, iodine, and aromatic hydrocarbons, which offer greater storage densities than traditional atomic propellants and potentially enable a greater total spacecraft impulse given the same propellant storage volume as gaseous atomic propellants [11–13]. While molecular propellants have great potential, recent experiments and studies show that common molecular propellants, such as nitrogen [14,15], air mixtures [16–18], and water [19,20], all exhibit highly degraded performance and efficiency compared to the more traditional atomic propellants.

Munro-O'Brien and Ryan tested a HET at low powers, 30–810 W, with common HET propellants and found that nitrogen exhibited the lowest anode efficiency at 5.4% compared to 9.6% for argon, 15.2% for krypton, and 26.3% for xenon [14]. Tejeda and Knoll tested xenon, water vapor, oxygen, and air in a HET at a moderate power level, 1520–1600 W, and measured anode efficiencies of 51.2%, 12.5%, 15.8%, and 15.1%, respectively. The results from this study once again demonstrate that HETs operated on molecular propellants significantly underperformed HETs operated on atomic propellants [19]. The low efficiencies in the molecular propellant tests were primarily attributed to poor mass utilization of the molecular propellants compared to the atomic propellants [14,19].

To influence more optimized thruster design in general and to better understand where certain thruster inefficiencies originate, Hofer [21,22] presented a phenomenological efficiency model, which Brown [23,24] expanded into an analytical efficiency model for atomic propellants in a HET. This model decomposes thrust efficiency into a series of efficiency terms that are independently empirically measured from diagnostics in the HET plume and, when multiplied together, result in the overall measured thrust efficiency. This analysis framework quantifies the effect of various energy sinks present within a HET, highlights the largest potential areas of improvement for thruster efficiency optimization, and offers a standard method to compare efficiencies between thrusters and atomic propellants.

While the existing atomic efficiency model fits well with experimental data and offers insight into areas of improvement for HET performance optimization, it is limited in that it is only valid for atomic propellants. The base assumptions of the atomic efficiency model, that all ionic species have the same mass and acceleration voltage, begin to break down when applied to molecular propellants. Furthermore, molecular propellants can dissociate and become rotationally and vibrationally excited [25], which are major energy sinks for molecular propellants that the atomic efficiency model does not consider. To develop more efficient molecular propellant HETs, these additional molecular energy sinks need to be better understood and quantified, which can be achieved through a modification of the atomic efficiency model to account for a changing ionic species mass and acceleration voltage.

This paper presents an updated analytical efficiency model that applies to molecular propellants to quantify the effect of the molecular

energy sinks and influence more optimized molecular propellant HET design. This molecular model is then applied to experimental data on a 5 kW HET to validate the molecular model and to quantify and better understand the sources of degraded thrust efficiency present in molecular propellants.

II. Efficiency and Energy Model of a Hall Thruster

The following subsections introduce the efficiency models for atomic and molecular propellants. The first subsection summarizes the atomic efficiency model developed by Hofer [21] and Brown [23]. To better visualize the energy pathways and pertinent energy sinks in an atomic propellant HET, an atomic energy flow model is introduced. The second subsection expands this energy flow model to hold for a diatomic propellant that captures the new energy pathways and energy sinks seen with molecular propellants. Finally, the last subsection derives the molecular efficiency model based on the new energy pathways and assumptions present with molecular propellants seen from the diatomic energy flow model.

A. Atomic Propellant Efficiency and Energy Flow Model

The existing atomic efficiency model analytically decomposes anode thrust efficiency (η_T), as defined in Eq. (1a), into energy (η_E), propellant (Φ_P), and beam efficiencies (Ψ_b) as outlined by Brown [23].

$$\eta_T = \frac{(1/2)T^2}{\dot{m}_a P_d} = \left\{ \frac{(1/2)\dot{m}_a \langle \bar{v}^2 \rangle_m}{P_d} \right\} \left\{ \frac{\langle \bar{v} \rangle_m^2}{\langle \bar{v}^2 \rangle_m} \right\} \{ \langle \cos \theta \rangle_{mv}^2 \} = \eta_E \Phi_P \Psi_b \quad (1a)$$

$$\eta_T = \frac{(1/2)T^2}{\dot{m}_a P_d} = \left\{ \frac{(1/2)\dot{m}_a \langle \bar{v}^2 \rangle_m}{P_d} \right\} \left\{ \frac{\langle \bar{v} \rangle_m^2}{\langle \bar{v}^2 \rangle_m} \right\} \{ \langle \cos \theta \rangle_{mv}^2 \} = \eta_E \Phi_P \Psi_b \quad (1b)$$

This equation begins with the standard definition of η_T , using thrust (T), mass flow rate to the anode (\dot{m}_a), and discharge power (P_d). Using the component-weighted formulation of thrust ($T = \dot{m}_a \langle \bar{v} \rangle_m \langle \cos \theta \rangle_{mv}$), this expression can be further expanded into a function of the averaged particle velocity (v) components and plume angular location (θ). In Eq. (1a), $\langle \rangle_m$ represents a mass-averaged quantity and $\langle \rangle_{mv}$ signifies a momentum-averaged quantity. Analytical expressions for η_E , Φ_P , and Ψ_b are derived through grouping the components of η_T as done in Eq. (1a).

η_E represents how effectively a thruster converts input power into jet power and can be expanded into a product of current utilization (η_b) and voltage utilization (η_v) as outlined in Eq. (2), with the assumption that all charge species are subject to the same acceleration voltage (V_a). At unity energy efficiency, current utilization and voltage utilization are also both unity. Unity current utilization is achieved when all cathode electrons neutralize the beam and no electrons make it to the anode, causing beam current (I_b) to equal discharge current (I_d). Unity voltage utilization is achieved when V_a is equivalent to the input discharge voltage (V_d), causing ions to be subject to the full acceleration potential.

$$\eta_E = \frac{(1/2)\dot{m}_a \langle \bar{v}^2 \rangle_m}{P_d} = \left\{ \frac{V_a}{V_d} \right\} \left\{ \frac{I_b}{I_d} \right\} = \eta_v \eta_b \quad (2)$$

Φ_P represents how effectively a thruster utilizes the propellant mass. At peak efficiency, a thruster ionizes the entire propellant mass to a single charge state, and deviations from this ideal state will result in a loss of propellant efficiency. Φ_P can be expanded into a charge utilization (Φ_q), mass utilization (Φ_m), and neutral-gain utilization (Φ_{N-G}) as seen in Eq. (3), with the assumption that all charge species have the same mass. In this equation, Ω_j is the current fraction of the j th charge species, Z_j is the charge state of the j th charge species, \dot{m}_i is the mass flow rate of the plume ions, y_0

is the average neutral speed normalized by average ion speed, and Q is the average ion charge state. This formulation of Φ_P is derived by separating the velocity components into a polydisperse ionization term, which becomes Φ_q , and the remainder of the weighted velocity components, which become a product of Φ_m and Φ_{N-G} . A detailed derivation of the $\Phi_m \Phi_{N-G}$ term can be found in Appendix B of Brown et al. [23].

$$\begin{aligned}\Phi_P &= \frac{\langle \bar{v} \rangle_m^2}{\langle v^2 \rangle_m} = \left\{ \frac{\langle \bar{v}_i \rangle_m^2}{\langle v_i^2 \rangle_m} \right\} \left\{ \frac{\langle \bar{v} \rangle_m^2 \langle v_i^2 \rangle_m}{\langle \bar{v}_i \rangle_m^2 \langle v^2 \rangle_m} \right\} \\ &= \left\{ \frac{\left[\sum_{j=1} \left(\frac{\Omega_j}{\sqrt{Z_j}} \right) \right]^2}{\sum_{j=1} \left(\frac{\Omega_j}{Z_j} \right)} \right\} \left\{ \left(\frac{\dot{m}_i}{\dot{m}_a} \right) \left(1 + 2y_o \frac{1 - \Phi_m}{\Phi_m \sqrt{Q\Phi_q}} \right) \right\} \\ &= \{\Phi_q\} \{\Phi_m\} \{\Phi_{N-G}\}\end{aligned}\quad (3)$$

Ψ_b captures the drop in overall efficiency due to the off-axis component of jet momentum, where at maximum efficiency the velocity vector of all accelerated ions will be aligned with the axial thrust vector. Ψ_b can generally be approximated using the measured axial beam current (I_{axial}) and beam divergence angle (θ_d), as shown in Eq. (4a), assuming that the charge species current fraction is constant across all plume angles.

$$\Psi_b = \langle \cos \theta \rangle_{\text{mv}}^2 \approx \left(\frac{I_{\text{axial}}}{I_b} \right)^2 = \cos^2 \theta_d \quad (4a)$$

$$\Psi_b = \langle \cos \theta \rangle_{\text{mv}}^2 \approx \left(\frac{I_{\text{axial}}}{I_b} \right)^2 = \cos^2 \theta_d \quad (4b)$$

A HET would operate at unity thrust efficiency if it converts all input power into plume jet power. However, in reality, this is never possible since thrusters contain energy sinks that prevent perfect energy conversion. Furthermore, input power is not converted directly into jet power but rather converts via a multistep process including transfer to electrons via cathode emission, subsequent transfer to heavy particles via electron–neutral collisions, and finally transfer to jet power via ion acceleration. With conservation of energy principles, input power can be tracked through a HET using an energy flow model as a graphical tool to more easily visualize where some of the energy sinks originate in each of these processes.

The analytical efficiency model serves to quantify the strength of various energy sinks and thus informs on the prominent energy sinks to include in the energy flow model. For example, η_E captures energy

sinks within electron processes, such as electronic excitation collisions and Joule heating, along with ion processes, such as incomplete ion acceleration. Φ_P captures energy sinks in processes involving heavy particles, such as thermal heating, ion/wall recombination, and polydisperse ionization. Finally, Ψ_b captures off-axis jet power due to off-axis ion acceleration and charge exchange (CEX) collisions. A representative energy flow diagram for an atomic propellant in a HET is shown in Fig. 1, where the corresponding efficiency term that relates to each energy sink is indicated. In this diagram, green represents the maximum efficiency path, orange represents an inefficient energy path that will still produce some thrust, and red represents an energy sink that will not produce thrust. This energy flow diagram presents a simplified interpretation of the endpoints where input power can emanate. For more intensive studies into specific energy sinks, the energy flow diagram can be modified to increase the fidelity of the intermediate processes related to the energy sink of interest. Additional studies are shown to directly measure some of these energy sinks [26–28].

As mentioned previously, the energy flow diagram is organized by the path through which input energy moves through a HET. The discharge power first transfers to electrons as they accelerate toward the discharge channel, where this power is either lost to the thruster body via electron–thruster collisions or transferred to neutral particles via electron–neutral collisions. After an electron collision, the neutral particles either ionize with sufficient energy and accelerate or excite one of their energy modes [29]. If all input energy travels along the green pathway in the energy flow diagram, the thruster would operate at maximum thrust efficiency, any energy that travels down an orange path will still produce some thrust but at the cost of reduced efficiency, and energy that travels down a red path causes a large reduction in thrust efficiency with no thrust produced.

B. Diatomic Propellant Energy Flow Model

In modifying the efficiency model to apply to molecular propellants, it is important to recognize any additional energy sinks or pathways that arise through the molecular ionization process to ensure the updated model accurately captures these processes. This can be seen through an expansion of the energy flow diagram to include molecular specific energy paths such as dissociation and excitation of the rotational and vibrational energy modes. The updated molecular energy flow diagram is shown in Fig. 2, where the corresponding efficiency terms will be introduced in the next section. In this figure, green represents the maximum efficiency path, orange represents an inefficient energy path that will still produce some thrust, and red represents an energy sink that will not produce thrust. For conciseness and simplicity, this energy flow diagram is shown for a diatomic molecule that can only ionize to a +1 charge state but could be further expanded for other non-

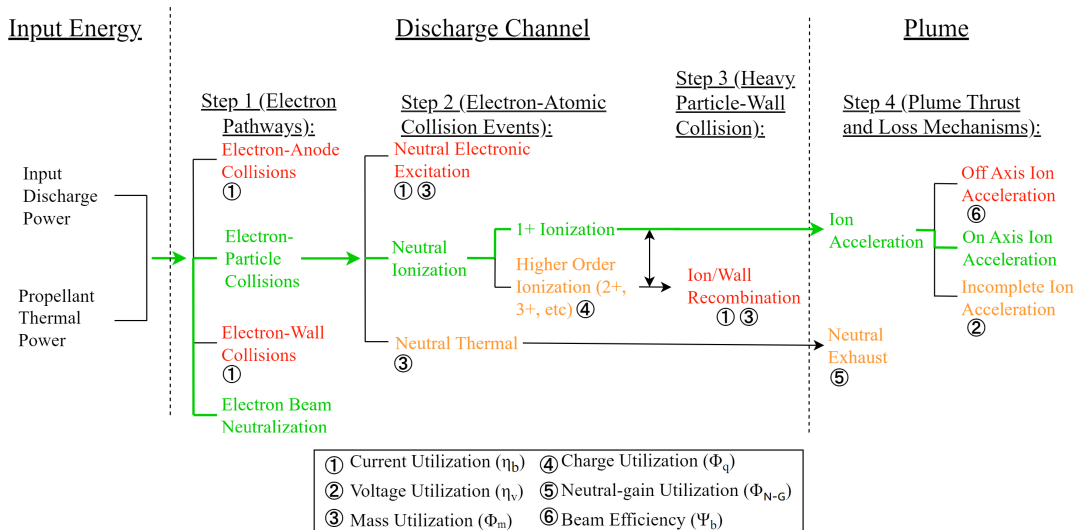


Fig. 1 Energy flow diagram of an atomic propellant in a HET.

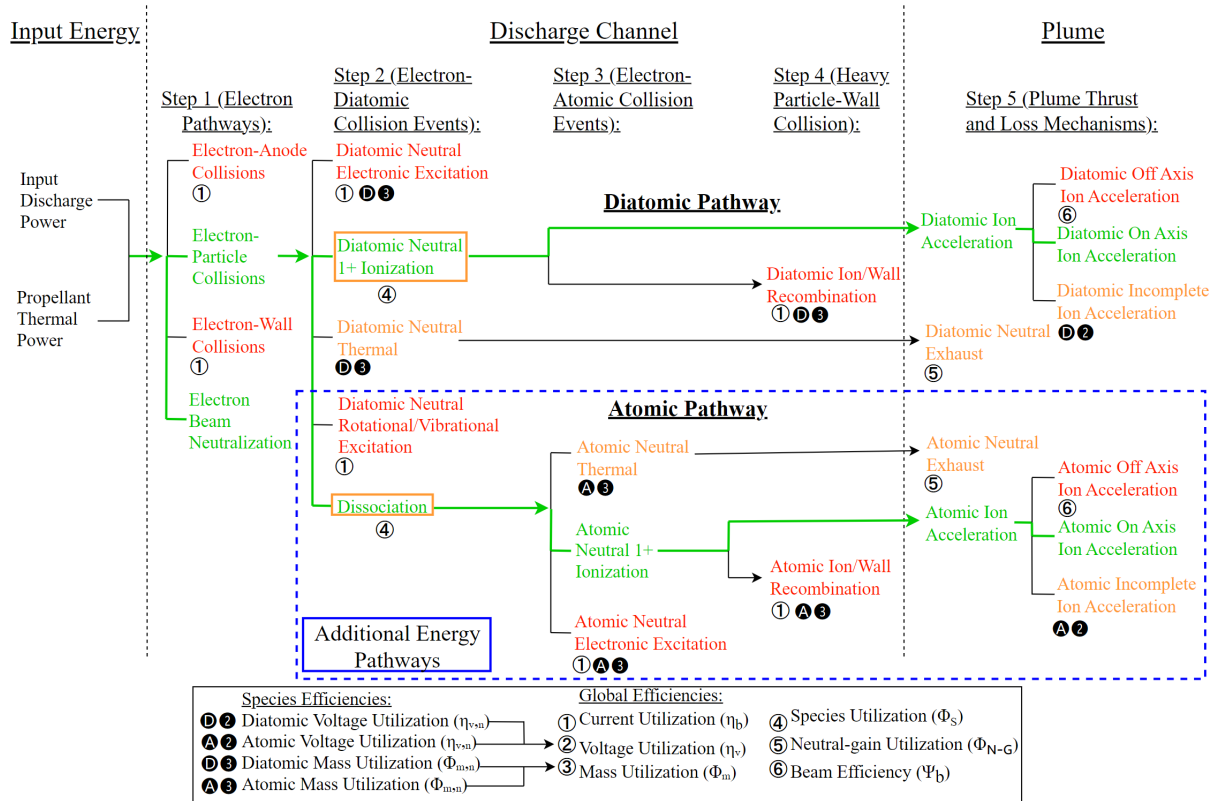


Fig. 2 Energy flow diagram of a diatomic propellant in a HET.

diatomic molecules and additional charge states. Note that Fig. 2 neglects higher-order ionization, which is generally a decent approximation for most molecular propellants, especially nitrogen and oxygen, due to their relatively high second ionization energies and extremely low second ionization cross sections [30].

Two immediate conclusions from the diatomic energy flow diagram are that the dissociation process greatly expands the number of potential energy pathways possible with molecular propellants and that there are two pathways that are designated as potentially efficient pathways. The presence of the dissociation mechanism splits the diatomic energy flow diagram into an atomic and diatomic pathway, which are visually similar in the diagram but, as will be seen later in this paper, possess energy sinks of different strengths. The input power will disperse among the available pathways as a function of the dominant electron-impact reaction mechanisms, physical properties of the diatomic propellant, and plasma properties within the discharge channel of the HET. The production of atomic and molecular ions employs distinct reaction mechanisms that have varying reaction rates. Furthermore, for diatomic propellants with relatively high bond energies, such as nitrogen, the production of atomic ions is generally a two-step dissociation and ionization process [31,32] compared to the one-step direct ionization process to create molecular ions [29]. These effects can generate a time delay in producing atomic ions that may force the atomic and molecular ions to experience different ionization and acceleration regions. This complex process allows each pathway to possess unique energy sinks, and for this reason, it is not immediately certain whether it is more efficient to produce atomic or molecular ions at a given thruster operating condition.

To compare the efficiencies between producing atomic and molecular ions from molecular propellants, the molecular efficiency model shall include both species and global efficiency terms. The “species” efficiency terms are composed of energy sinks specific to each individual species and are used to describe the relative efficiencies between producing different species from a molecular propellant (e.g., Is it more efficient to produce N_2^+ or N^+ with nitrogen propellant?). As seen in the molecular energy flow model, there are multiple potentially efficient energy pathways for a molecular propellant, and

the species efficiency terms will allow for a direct quantitative comparison of the efficiency between different ionic species produced, such as N_2^+ and N^+ in a nitrogen propellant. “Global” efficiency terms, on the other hand, will be defined as functions of species efficiency terms and allow for the direct comparison of efficiency terms between different molecular propellants and between atomic and molecular propellants. Atomic propellants have one distinct efficient energy pathway, and some molecular propellants can have more than the two seen in a diatomic propellant (e.g., CO_2 can form CO_2^+ , O_2^+ , O^+ , etc.). Global efficiency terms from the molecular efficiency model are analogous to the efficiency terms from the existing atomic efficiency model and enable direct efficiency comparisons between propellants with different ionization pathways, such as nitrogen, carbon dioxide, and argon.

C. Molecular Propellant Efficiency Model

The intent of the molecular efficiency model is to provide a framework in which to analyze the efficiency breakdown of a HET operating on a molecular propellant. The analytical decomposition of anode thrust efficiency into various efficiency terms will highlight the dominant energy sinks that cause degradations in the resultant efficiency. Furthermore, given a change in measured efficiency between thruster setpoints, molecular propellants, or HETs, this model will show the underlying mechanisms for why there is a change in efficiency. Additionally, this model informs on the recommended diagnostics to use when analyzing molecular propellant operation in a HET.

The derivation of the following molecular propellant efficiency model has the following three new base assumptions compared to the atomic model: 1) each ionic species can be subject to a different acceleration voltage, 2) each species can have a different mass, and 3) all ionic species have a + 1 charge. Assumptions (1) and (2) differ from the atomic model due to the ability of the molecule to dissociate and vary its mass and potentially have a noticeably different ionization/acceleration region for each ionic species. Assumption (3), as mentioned in the previous section, holds for most molecular propellants due to the low probability of producing multiply-charged

ions from molecular propellants. This modified molecular efficiency model holds for all molecular propellants, not just diatomic molecules, assuming that they approximately meet the above assumptions. The derivation of the molecular efficiency model is similar to the atomic model in that η_T is once again decomposed into energy, propellant, and beam efficiency, as shown in Eq. (1b), which has been reproduced here from Sec. II.A. for clarity.

Each of these efficiencies has a similar interpretation as they do in the atomic model; however, they have different functional forms. Note that η_E , the global energy efficiency, can be reduced to the summation of the product of species voltage utilization ($\eta_{V,n} = (V_{a,n}/V_d)$) and species current utilization ($\eta_{b,n} = (I_{b,n}/I_d)$), as seen in Eq. (5). $V_{a,n}$ is the acceleration voltage applied to the n th species and $I_{b,n}$ is the beam current of the n th species.

$$\begin{aligned}\eta_E &= \frac{(1/2)\dot{m}_a \langle \bar{v}^2 \rangle_m}{P_d} = \left\{ \frac{(1/2)\langle \bar{v}_i^2 \rangle_m}{V_d} \right\} \left\{ \frac{\langle \bar{v}^2 \rangle_m}{\langle \bar{v}_i^2 \rangle_m} \right\} \left\{ \frac{\dot{m}_a}{I_d} \right\} \\ &= \frac{V_{a,1} I_{b,1}}{V_d I_d} + \frac{V_{a,2} I_{b,2}}{V_d I_d} + \dots = \sum_{n=0} \eta_{V,n} \eta_{b,n}\end{aligned}\quad (5)$$

In the Φ_P derivation for molecular propellants, Φ_q is assumed unity due to the assumption that all ionic species have $a + 1$ charge state. However, since the constant mass assumption is relaxed, a new efficiency term is introduced, denoted as species utilization (Φ_s). This term is similar to the interpretation of Φ_q in that it accounts for the inefficiency seen with polydisperse ionization. Φ_s is unity when all ions are of the same mass species and will fall below unity with the production of ionic species of differing mass states. Φ_P can then be decomposed into Φ_s , Φ_m , and Φ_{N-G} as seen in Eq. (6). Some additional new terms that emerge are species mass utilization ($\Phi_{m,n} = (\dot{m}_{i,n}/\dot{m}_n)$) and species fraction ($\xi_n = (\dot{m}_n/\dot{m}_a)$). Note that $\dot{m}_{i,n}$ is the mass flow rate of the n th ionic species, and \dot{m}_n is the total mass flow rate of the n th species, including contributions from both neutral and ionic mass flow rates. The resultant terms for Φ_s , Φ_m , and Φ_{N-G} are presented in Eqs. (7–9), respectively.

$$\Phi_P = \frac{\langle \bar{v}_i^2 \rangle_m}{\langle \bar{v}^2 \rangle_m} = \frac{\langle \bar{v}_i^2 \rangle_m}{\langle \bar{v}_i^2 \rangle_m} \cdot \left[\frac{\langle \bar{v}_i^2 \rangle_m}{\langle \bar{v}_i^2 \rangle_m} \cdot \frac{\langle \bar{v}^2 \rangle_m}{\langle \bar{v}^2 \rangle_m} \right] = \Phi_s \Phi_m \Phi_{N-G} \quad (6)$$

$$\Phi_s = \frac{\langle \bar{v}_i^2 \rangle_m}{\langle \bar{v}_i^2 \rangle_m} = \frac{\langle \sqrt{\mathcal{M}_n \eta_{V,n}} \rangle_I^2}{\langle \mathcal{M}_n \rangle_I \langle \eta_{V,n} \rangle_I} = \frac{\left(\sum_{n=0} \Omega_{i,n} \sqrt{\mathcal{M}_n \eta_{V,n}} \right)^2}{\sum_{n=0} \Omega_{i,n} \mathcal{M}_n \sum_{n=0} \Omega_{i,n} \eta_{V,n}} \quad (7)$$

$$\Phi_m = \frac{\dot{m}_i}{\dot{m}_a} = \sum_{n=0} \Phi_{m,n} \xi_n \quad (8)$$

$$\Phi_{N-G} = \left(\frac{\sum_{n=0} \xi_n (1 - \Phi_{m,n}) \bar{v}_{0,n}}{\sum_{n=0} \xi_n \Phi_{m,n} \bar{v}_{i,n}} + 1 \right)^2 \quad (9)$$

In the above equations, \mathcal{M}_n is the molar mass of the n th species, $\Omega_{i,n}$ is the current fraction of the n th species, $\bar{v}_{0,n}$ is the average neutral velocity of the n th species, and $\bar{v}_{i,n}$ is the average ion velocity of the n th species. The expression for beam efficiency has the same form and interpretation as in the atomic model as seen in Eq. (4b), and it has been reproduced from Sec. II.A for clarity.

To compare the relative efficiencies between the production of different ionic species in a molecular propellant, a new efficiency term is defined and denoted as species parameter efficiency (η_{SP}), as shown in Eq. (10). While η_{SP} is not derived analytically from η_T similar to the other efficiency terms, it is useful in that it contains the largest contributing species efficiency terms, and it can be used as a quantitative metric to determine the most efficient ionization pathway for a molecular propellant. For example, with a nitrogen

propellant, η_{SP} will indicate if it is more efficient to produce N^+ or N_2^+ species, which likely experience different ionization and acceleration regions and possess energy sinks of varying strengths. Note that $\eta_{b,n}$ is not included in this formulation because many of the processes that contribute to decreased η_b , such as electron–wall collisions and anomalous electron mobility, cannot be attributed to a specific species and the $\eta_{b,n}$ term emerges mainly as a product of the averaging process. Note that, as more diagnostics are included that can measure species specific energy sinks in greater fidelity, additional components can be added to the formulation of η_{SP} to account for these contributions.

$$\eta_{SP} = \eta_{V,n} \Phi_{m,n} \quad (10)$$

In the derived molecular efficiency model, η_E , Φ_P , and η_E are global efficiency terms, which can be directly compared between different propellants, including atomic and molecular, to grant additional insight into how propellant selection affects the relative strength of various HET energy sinks. Note that $\eta_{V,n}$, $\Phi_{m,n}$, and η_{SP} , on the other hand, are species efficiency terms, which can be directly compared between the species produced from a molecular propellant. The species efficiency terms provide information on how the strength of certain HET energy sinks is distributed among all the species produced and which ionization pathway is the most efficient.

III. Experimental Design and Setup

The following subsections overview the test design and diagnostics used to collect the data. This includes the thruster operational setpoints chosen, characteristics of the chamber and thruster used, and test configuration of each of the diagnostics. This section concludes with a discussion of probe corrections to account for background pressure and an approximation for the species fraction term.

A. Test Overview

The authors performed an experimental test to illustrate the molecular efficiency model and how this model details energy sinks within a HET. For a representative molecular propellant, the authors chose nitrogen due to its prevalence in air-breathing electric propulsion and inert nature, and for comparative atomic propellants, the authors chose argon and xenon. Argon is the atomic propellant most similar to nitrogen in terms of mass, ionization energy, and ionization cross section [33], and it will provide the most direct comparison of nitrogen's distinct molecular contributions on efficiency. Xenon is historically the most commonly used atomic propellant, and for this reason will also provide a good comparison for nitrogen. The nitrogen efficiency is analyzed using the molecular efficiency model presented in Sec. II.C., while argon and xenon were analyzed with the atomic efficiency model outlined in the work of Brown [23] and presented in Sec. II.A. Table 1 presents an outline of the mass, first ionization energy, and dissociation energy of all species present in this experiment [34,35].

For each setpoint, mass flow rate and discharge voltage are matched between the propellants. V_d is matched to approximately maintain a similar electron temperature (T_e) in the discharge channel [29]. Since \dot{m}_a is a prominent term in thrust, specific impulse, and efficiency, keeping \dot{m}_a constant will instead allow for the analysis of how the physical properties of the propellants, including the specific molecular contributions of nitrogen, influence changes in the major performance metrics. The range of mass flow rates and

Table 1 Species properties

Species	Mass, amu	First ionization energy, eV	Dissociation energy, eV
Xe	131.29	12.13	—
Ar	39.95	15.76	—
N ₂	28.02	15.58	9.76
N	14.01	14.53	—

discharge voltages tested are based on the exhibited stable region of the thruster operating on nitrogen, as nitrogen has the narrowest stability region. For discharge voltages above 275 V and below 225 V, the HET becomes unstable and cannot sustain a discharge on nitrogen. For each propellant, the magnetic field is adjusted to minimize discharge current and discharge current peak-to-peak oscillations and then kept constant for the remainder of the setpoints. The chosen setpoints (N3, Ar3, and Xe3) to optimize the magnetic field are selected since they share the most common operational conditions with the rest of the setpoints. The setpoint operating conditions for nitrogen, argon, and xenon are outlined in Tables 2–4, respectively. For all setpoints, the cathode operates with xenon as the cathode gas, which is maintained at 4.5 sccm. This cathode setpoint was selected in preliminary testing, as it is the lowest flow rate that maintains stable HET operation across all propellants and setpoints to minimize potential xenon ingestion into the thruster. In the following tables, the peak radial magnetic field is measured in the center of the discharge channel at the thruster exit plane.

B. Vacuum Test Facility and Thruster

All measurements for the investigation are performed in Vacuum Test Facility 1 (VTF-1) at the High-Power Electric Propulsion Lab (HPEPL) at Georgia Tech. VTF-1 measures 7 m in length by 4 m in diameter and reaches high vacuum using a set of six 48" diffusion pumps. With the diffusion pumps, VTF-1 achieves a base pressure of 1×10^{-6} Torr, operational pressures between 1.1×10^{-5} and 4.5×10^{-5} Torr corrected for the respective gas, and a maximum calculated effective pumping speed of 292,000 l/s of N_2 . Pressure measurements were taken using an SRS IGC100 ion gauge controller and Kurt J. Lesker G100F ion gauge located coincident to the exit plane of the thruster, and the calculation for effective pumping speed is based on the best practice pressure guidelines [36]. Tables 2–4 present the operational pressure for each setpoint, and Fig. 3 illustrates the layout of the chamber along with probe positioning for this test.

The thruster used for all setpoints in this test campaign is the P5 5-kW HET. Gulczinski [37] presents the engineering drawings of the P5, which is described in detail and is configured as outlined in the work of Haas [38]. The P5 uses an EPL HCPEE 500 externally mounted cathode for all setpoints, positioned at the 12 o'clock position with the orifice located 2.2 cm downstream of the thruster exit plane and 14.7 cm above the thruster centerline. A Regatron TC.P.10.1000.480.S.HMI TopCon Quadro power supply supplied the discharge power, and TDK-Lambda power supplies powered the magnets (type GEN 40–38), cathode heater (type GEN 20–76), and keeper (type GEN 150–10). The P5 operates with a discharge filter installed, with a resistance value of 1.4 Ω in series and capacitance of 79.7 μF in parallel to the discharge circuit.

The authors selected the P5 for this test due to its designed robustness as a laboratory thruster, relatively long 32 mm discharge channel length compared to most other midpower thrusters, which effectively increases the residence time of the lightweight nitrogen particles in the discharge channel, and myriad of comparative historical performance data. Historically, the P5 has operated primarily on xenon propellant at mass flow rates from 5.25 to 15 mg/s and discharge voltages of 200–600 V with presented performances of 65–400 mN of thrust, 1000–2700 s of specific impulse, and anode thrust efficiencies of 34–56% [22,37–39]. To the author's knowledge at the time of publication, no other groups have operated the P5 on argon or nitrogen propellants. Some historical data is presented later, alongside the data from this experiment, in the results sections of this paper. Note that the xenon setpoints in this test have a mass flow rate of 5 mg/s, which is off-nominal from what has been run historically but is chosen to match the mass flow rate of the stable setpoints of nitrogen. The thruster body is electrically floated for all setpoints.

MKS GE50A mass flow controllers (MFCs) meter the anode and cathode, and their operational flow rates are calibrated with a MesaLabs DryCal 800. The MFCs have an uncertainty of 1% of the current setpoint, leading to a maximum test uncertainty of ± 0.05 mg/s.

Table 2 HET operational setpoints on nitrogen

Setpoint	Anode flow rate [N_2], mg/s (sccm)	Cathode flow rate [Xe], mg/s (sccm)	Discharge voltage, V	Discharge power, kW	Peak radial B-field, G	Chamber pressure, (Torr, N_2)
N1	5.0 (240)	0.44 (4.5)	231.9	3.08	130	1.47×10^{-5}
N2	5.0 (240)	0.44 (4.5)	255.1	3.69	130	1.14×10^{-5}
N3	5.0 (240)	0.44 (4.5)	278.6	4.30	130	1.19×10^{-5}
N4	5.2 (250)	0.44 (4.5)	277.0	4.56	130	1.38×10^{-5}
N5	5.4 (260)	0.44 (4.5)	275.7	4.81	130	2.14×10^{-5}

Table 3 HET operational setpoints on argon

Setpoint	Anode flow rate [Ar], mg/s (sccm)	Cathode flow rate [Xe], mg/s (sccm)	Discharge voltage, V	Discharge power, kW	Peak radial B-field, G	Chamber pressure, (Torr, Ar)
Ar1	5.0 (168.3)	0.44 (4.5)	229.1	3.34	130	2.41×10^{-5}
Ar2	5.0 (168.3)	0.44 (4.5)	253.7	3.75	130	2.55×10^{-5}
Ar3	5.0 (168.3)	0.44 (4.5)	278.9	4.13	130	1.22×10^{-5}
Ar4	5.2 (175.3)	0.44 (4.5)	277.5	4.36	130	2.98×10^{-5}
Ar5	5.4 (182.4)	0.44 (4.5)	276.1	4.58	130	4.15×10^{-5}
Ar6	5.0 (168.3)	0.44 (4.5)	303.6	4.68	130	2.39×10^{-5}

Table 4 HET operational setpoints on xenon

Setpoint	Anode flow rate [Xe], mg/s (sccm)	Cathode flow rate [Xe], mg/s (sccm)	Discharge voltage, V	Discharge power, kW	Peak radial B-field, G	Chamber pressure, (Torr, Xe)
Xe1	5 (50.9)	0.44 (4.5)	230.8	1.75	162.5	4.49×10^{-5}
Xe2	5 (50.9)	0.44 (4.5)	250.3	2.15	162.5	3.94×10^{-5}
Xe3	5 (50.9)	0.44 (4.5)	274.3	2.03	162.5	3.28×10^{-5}

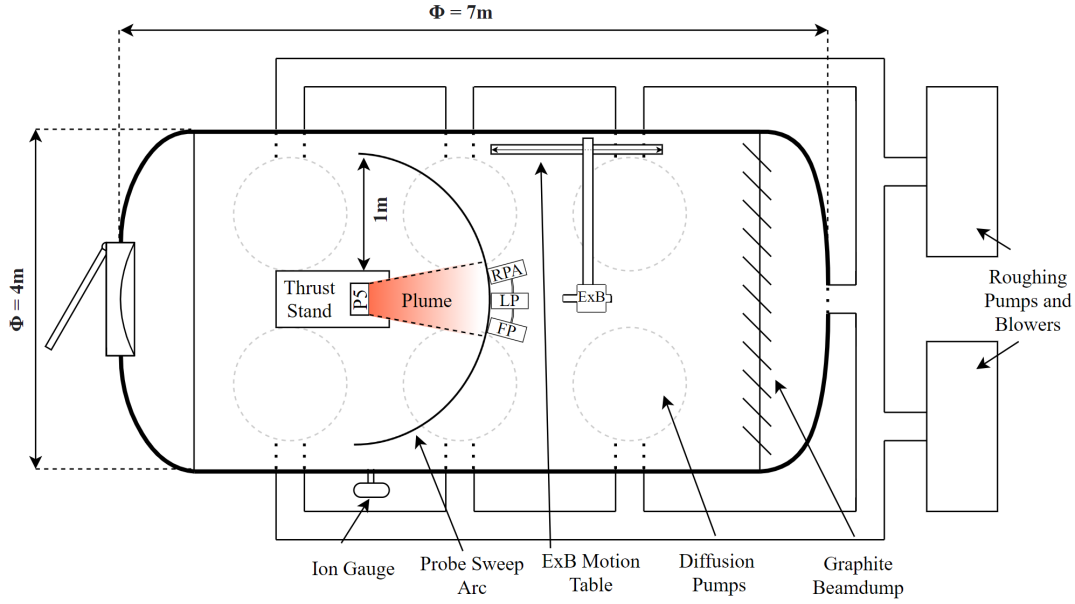


Fig. 3 Schematic of VTF-1.

C. Diagnostics

Thrust is measured using a null-type inverted pendulum thrust stand fitted with a TE Connectivity HR 100 linear varying differential transformer (LVDT). The thrust stand is configured and operated as detailed in the recommended practices for thrust measurements [40]. An installed calibration string calibrates the thrust stand signal and is set to a range of 0–194.7 mN for this test, which is based on the predicted thrust response of all propellants. This thrust measurement setup results in a maximum test uncertainty of ± 2.6 mN for nitrogen, ± 4.3 mN for argon, and ± 4.9 mN for xenon.

An $E \times B$ probe, or Wien filter, measures the charge and mass species current fractions along with the species' specific acceleration voltage for nitrogen. This probe is mounted on a two-axis Parker Daedal 803-9922A linear motion table, configured as outlined in the works of Kim and Gallimore [41] and Gurciullo et al. [42], and positioned 1 m downstream of the thruster exit plane on the thruster centerline for all measurements. $\Omega_{i,n}$ is calculated using a bi-Gaussian fit of the current trace as recommended in literature [42,43]. $V_{a,n}$ for each species is calculated according to Eq. (11) as a function of plate voltage at the n th species peak ($\Delta V_{\text{plate},n}$), plate separation distance (d), particle mass of the n th species (m_n), elementary charge of a $+1$ ion (e), and applied $E \times B$ magnetic field (B) [42], corrected by local plasma potential (V_p). Note that $\dot{m}_{i,n}$ is then calculated using Eq. (12), where \mathcal{F} denotes Faraday's constant. These methods result in a maximum $\Omega_{i,n}$ uncertainty of ± 0.05 for nitrogen, ± 0.07 for argon, and ± 0.10 for xenon and maximum $V_{a,n}$ uncertainty of ± 11.6 V.

$$V_{a,n} = \frac{m_n}{2eZ_j} \left(\frac{\Delta V_{\text{plate},n}}{dB} \right)^2 - V_p \quad (11)$$

$$\dot{m}_{i,n} = \frac{\Omega_{i,n} I_b \mathcal{M}_n}{\mathcal{F}} \quad (12)$$

A Langmuir probe, Faraday probe, and retarding potential analyzer (RPA) are installed on a theta probe arm that sweeps from -90° to $+90^\circ$ at 1 m downstream of the thruster exit plane as shown in Fig. 3. The Langmuir probe is a cylindrical type, constructed with a 0.11-mm-diameter tungsten filament with a length of 14.8 mm, where voltage is supplied and current measured using a Keithley 2470 Sourcemeter. For this dataset, the Langmuir probe measures V_p with the processes outlined in the work of Lobbia [44], resulting in a maximum measurement uncertainty of ± 0.25 V for all propellants.

The Faraday probe is a JPL nude type with a 22-mm-diameter tungsten-coated aluminum collector separated with a 1.15 mm gap from an aluminum guard ring, as presented by Frieman et al. [45] and Walker et al. [46]. This is swept from -90° to 90° , at an angular spacing of 0.2° , in a 1-m-radius arc with a collector potential of -50 V with respect to ground, where the voltage is supplied and current measured using a Keithley 2470 Sourcemeter. Beam current and beam divergence are postprocessed from the Faraday measurements using standard procedures and equations [47]. I_b maintains a maximum measurement uncertainty of ± 0.34 A for nitrogen, ± 0.48 A for argon, and ± 0.46 A for xenon, and the method to quantify θ_d uncertainty is discussed in Sec. III.D. Due to asymmetries in the plume, beam current is calculated using measurements from -90° to 0° and 0° to $+90^\circ$, then averaged for the resultant total beam current.

The RPA configuration consisted of a five-grid layout, with a floating grid, two electron suppression grids biased at -50 V with respect to ground, an ion repulsion grid that swept from 0 to $(V_d + 50)$ V, and copper collector grid as detailed by Xu [48]. A Keithley 2470 Sourcemeter supplied the voltage to the ion repulsion grids in increments of 1 V, a Xantrex XPD 60-9 power supply held the -50 V potential on the electron repulsion grids, and a Keithley 6485 Picoammeter measured the current from the collector. The RPA measures V_a , corrected by V_p , for xenon and argon, resulting in a maximum uncertainty of ± 4.4 V for argon and ± 4.5 V for xenon.

D. Background Pressure Corrections of Probe Data

Background neutrals and charge exchange collisions can cause T , I_d , I_b , and θ_d to be artificially higher than in ideal vacuum conditions [41,49,50]. Typically, these quantities are corrected for elevated pressures by varying chamber pressure to find the approximately linear relationship between these quantities and background pressure. This relationship is then extrapolated to a perfect vacuum condition [24,47]. Since VTF-1 has a relatively higher operational pressure, this method is not feasible for this test. The data is instead corrected by using a neutral ingestion model that is proposed by Randolph [51] and modified by Reid [52] and Brown [24]. Brown compared the neutral ingestion model approach to the more commonly used method of varying background pressure across four thruster setpoints ($V_d = 150$ V, 300 V and $\dot{m}_a = 10$ mg/s, 20 mg/s) and found the neutral ingestion model approach to be accurate within $\pm 1\%$ when compared to the method of varying chamber pressure [24]. In this model, the entrained background neutral mass flow rate (\dot{m}_{en}) into the discharge channel is approxi-

mated using the kinetic particle flux equation across a hemisphere centered at the thruster exit plane and reduced into Eq. (13).

$$\dot{m}_{\text{en}} = A_{\text{en}} P \sqrt{\frac{m_n}{2\pi k T_0}} \quad (13)$$

A_{en} is the area of the hemisphere, calculated as 488 cm² for the P5; P is the background chamber pressure in Pa; k is Boltzmann's constant; and T_0 is the temperature of the background neutrals, which is assumed to be 300 K. The entrained flow is then assumed to be ionized and accelerated into the beam, which causes the artificial increase in I_d , I_b , and T . The actual entrained mass flow can vary from what is presented in Eq. (13), and entrained mass that is ionized generally does not contribute as much to thrust as mass that originates from the anode, so an area entrainment factor (ζ_A) and thrust entrainment factor (ζ_{en}) are introduced as corrections to match empirical data trends. The equations for corrected I_d , I_b , and T are shown in Eqs. (14–16), respectively [24].

$$I_{d,\text{corr}} = I_d - \zeta_A \dot{m}_{\text{en}} \frac{e}{m_n} \quad (14)$$

$$I_{b,\text{corr}} = I_b - \zeta_A \dot{m}_{\text{en}} \frac{e}{m_n} \quad (15)$$

$$T_{\text{corr}} = T \left(1 - \zeta_{\text{en}} \frac{\dot{m}_{\text{en}}}{\dot{m}_a + \dot{m}_{\text{en}}} \right) \quad (16)$$

The correction factors are set to $\zeta_A = 1.0$ as is done in the work of Reid [52] and $\zeta_{\text{en}} = 0.8$, which is scaled by power and mass flow trends seen in the work of Brown [24] for the conditions in this test. Beam divergence is corrected for CEX collisions by recording the beam current density measurements at $\pm 90^\circ$ and subtracting these values out across all plume angles. This correction method, as described by Azziz [53], provides a lower limit for θ_d and assumes that all current measured at $\pm 90^\circ$ is CEX current and this current is distributed evenly across all angles. An upper limit on θ_d is determined by using the raw Faraday data with no CEX corrections. The recorded value for θ_d is the average of these two methods, and the error bounds due to CEX corrections were set based on these upper and lower limits. Error propagation for all diagnostics is performed by using standard methods outlined in NIST Technical Note 1297 [54], with maximum calculated uncertainties for each measured quantity summarized in Table 5.

E. Species Fraction Approximation

With the current set of plasma diagnostics used for this experiment, ξ_n is not directly measured since biased plasma probes cannot detect the neutral particles that contribute to ξ_n . The value for ξ_N , being the species fraction for atomic nitrogen, for this test is approximated using Eq. (17). $\dot{m}_N/\dot{m}_{i,N_2}$ from this equation is assumed to be a function of the reaction rates of the nitrogen dissociation mechanism ($\partial n_N/\partial t$) and ionization mechanism ($\partial n_{N_2^+}/\partial t$) at a given T_e as seen in Eq. (18) [55].

$$\xi_N = \frac{\dot{m}_N}{\dot{m}_a} = \left\{ \frac{\dot{m}_N}{\dot{m}_{i,N_2}} \right\} \left\{ \frac{\dot{m}_{i,N_2}}{\dot{m}_a} \right\} = \left\{ \frac{\dot{m}_N}{\dot{m}_{i,N_2}} \right\} \left\{ \frac{\Omega_{i,N_2} I_b \mathcal{M}_{N_2}}{\dot{m}_a \mathcal{F}} \right\} \quad (17)$$

$$\frac{\dot{m}_N}{\dot{m}_{i,N_2}} \approx \frac{(\partial n_N/\partial t) m_N}{(\partial n_{N_2^+}/\partial t) m_{N_2^+}} = \frac{(2K_{d,N_2} N_{N_2} n_i) m_N}{(K_{i,N_2} N_{N_2} n_i) m_{N_2^+}} = \frac{K_{d,N_2}}{K_{i,N_2}} \quad (18)$$

In Eq. (18), N_{N_2} is the neutral number density of molecular nitrogen, n_i is the plasma density, K_{d,N_2} is the reaction rate constant of the primary nitrogen dissociation mechanism ($e^- + N_2 \rightarrow 2N + e^-$), and K_{i,N_2} is the reaction rate constant of the primary molecular nitrogen ionization mechanism ($e^- + N_2 \rightarrow N_2^+ + 2e^-$). The reaction rate constant of the k th mechanism (K_k), in turn, is calculated using Eq. (19), as a function of the mass of an electron (m_e), energy of an impacted electron (ϵ_e), reaction energy of the k th reaction mechanism (ϵ_k), cross section of the k th mechanism (σ_k), and normalized electron energy distribution function (f_e) [56,57].

$$K_k = \sqrt{\frac{2}{m_e}} \int_{\epsilon_k}^{\infty} \sigma_k(\epsilon_e) \sqrt{\epsilon_e} f_e d\epsilon_e \quad (19)$$

In the above equations, f_e is assumed Maxwellian at a given T_e . Ionization cross sections for this analysis are obtained from Itikawa [58], and dissociation cross sections are obtained from Cosby [59]. For nonmagnetically shielded HETs operating on xenon, T_e in the discharge channel is estimated to be approximately 0.1 V_d [29,60,61]. T_e in low-temperature plasmas is seen to scale with reduced electric field (E/N), where (E) is the strength of the local electric field, and (N) is the neutral density [62]. Since \dot{m}_a is matched between each of the propellants, there will be a different N due to the differences in their masses. Therefore, the corrected electron temperature for nitrogen (T_{e,N_2}) is approximated, as shown in Eq. (20), where \bar{c}_n is the average thermal velocity of the n th species, calculated as $\bar{c}_n = \sqrt{(8kT/\pi m_n)}$.

$$\begin{aligned} T_{e,N_2} &\approx T_{e,\text{Xe}} \frac{(E/N)_{N_2}}{(E/N)_{\text{Xe}}} \approx \frac{0.1 V_d}{N_{N_2}/N_{\text{Xe}}} \approx 0.1 V_d \frac{\dot{m}_{a,\text{Xe}} m_{N_2} \bar{c}_{\text{Xe}}}{\dot{m}_{a,N_2} m_{\text{Xe}} \bar{c}_{N_2}} \\ &= 0.1 V_d \sqrt{\frac{m_{N_2}}{m_{\text{Xe}}}} \end{aligned} \quad (20)$$

This approximation for ξ_N has limitations in that it assumes that dissociation and ionization occur in the same region of the discharge channel at a constant T_e , the primary dissociation mechanism ($e^- + N_2 \rightarrow 2N + e^-$) produces all dissociated species, and the primary molecular ionization mechanism ($e^- + N_2 \rightarrow N_2^+ + e^-$) produces all molecular ions. For future experiments, ξ_N can be more accurately measured using optical emission spectroscopy (OES) or two-photon absorption laser-induced fluorescence (TALIF) at the thruster exit plane, where both techniques have been performed before for flowing nitrogen plasmas [31,63–65].

IV. Results and Discussion

The following subsections present the test results from the setpoints and analysis methods mentioned in the previous section. The first subsection focuses on overall performance trends measured in this experiment, and the subsequent subsections analyze the results from the atomic and molecular efficiency models applied to this dataset and how discharge voltage affects the individual efficiency parameters. Figure 4 shows operational pictures of the P5 firing on each propellant.

A. Overall Performance Trends

The overall performance metrics of thrust, specific impulse (I_{sp}), and thrust efficiency, as calculated from thrust measurements, are presented for all setpoints and propellants in Figs. 5–7, respectively. Historical data from the P5 thruster on xenon are superimposed on

Table 5 Maximum diagnostic uncertainty using standard error propagation

Propellant	T	Ω_{in}	V_p	I_b	θ_d	$V_{a,n} (E \times B)$	V_a (RPA)
Nitrogen	± 2.6 mN	± 0.05	± 0.25 V	± 0.34 A	$\pm 3.3^\circ$	± 11.6 V	—
Argon	± 4.3 mN	± 0.07	± 0.25 V	± 0.48 A	$\pm 3.2^\circ$	—	± 4.4 V
Xenon	± 4.9 mN	± 0.10	± 0.25 V	± 0.46 A	$\pm 4.4^\circ$	—	± 4.5 V

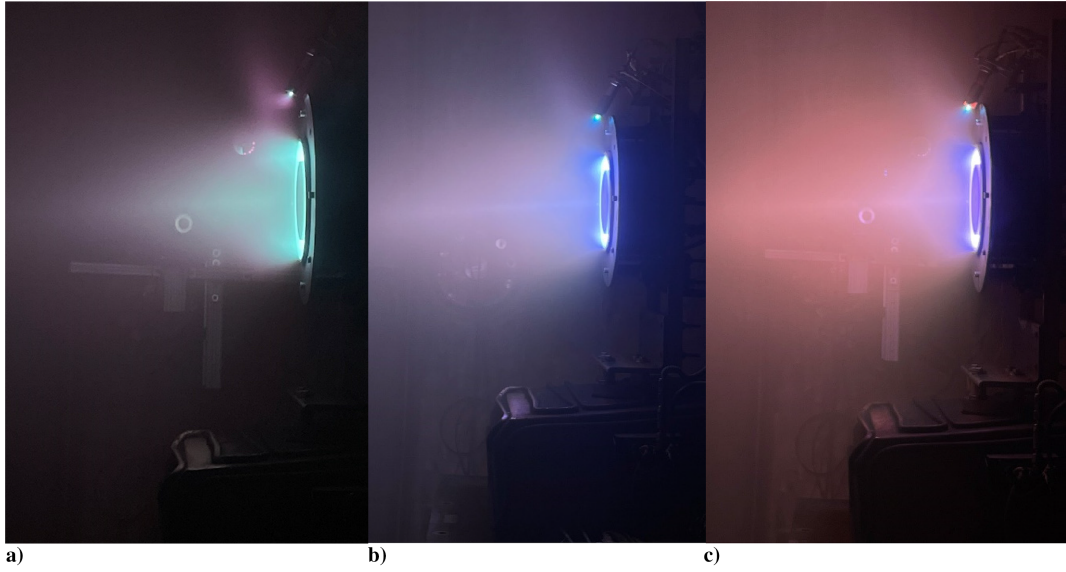


Fig. 4 P5 operating on xenon (a), argon (b), and nitrogen (c) propellant.

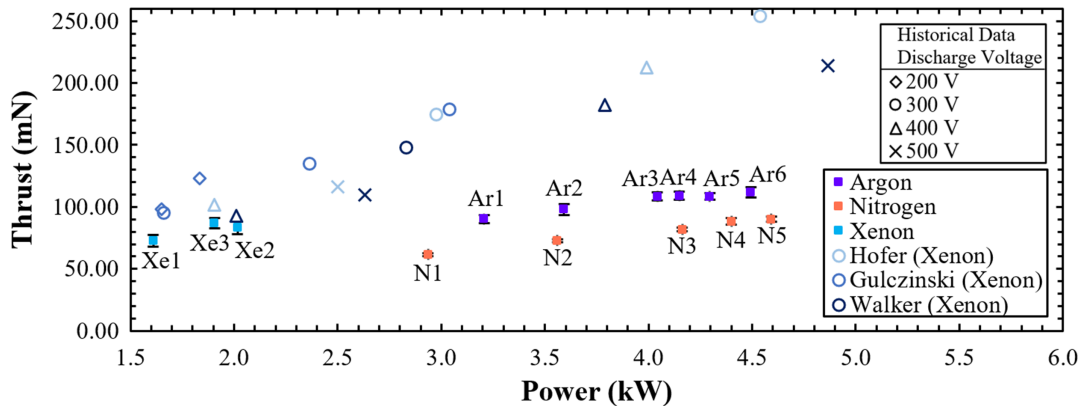


Fig. 5 P5 HET thrust as a function of discharge power on xenon, argon, and nitrogen. All historical data was run on xenon.

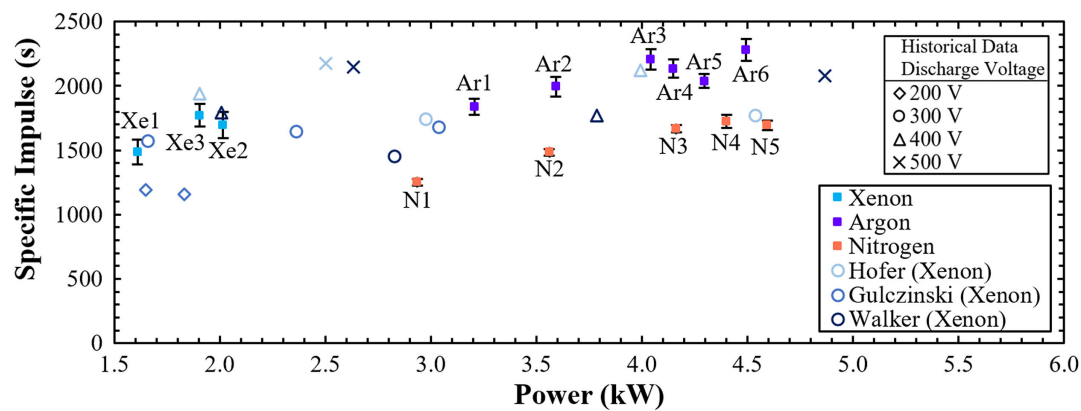


Fig. 6 P5 HET specific impulse as a function of discharge power on xenon, argon, and nitrogen. All historical data was run on xenon.

these plots to verify the xenon points still match historical trends, even though they are taken at an off-nominal low mass flow rate. The historical data also scales with power to allow comparisons at similar power levels with present argon and nitrogen data. In these figures, VTF-1 data has an \dot{m}_a range of 5.0–5.4 mg/s and V_d range of 229–304 V, and the historical data has \dot{m}_a and V_d ranges of 5.3–14.6 mg/s and 300–500 V (Hofer) [22], 5.7–10.3 mg/s and 200–300 V (Gulczinski) [37], and 5.3–10.5 mg/s and 300–500 V (Walker) [39], respectively. It is important to note that no resolvable xenon traces were detected with the $E \times B$ for the argon and nitro-

gen setpoints, and any contributions to performance from ingested xenon cathode gas are assumed to be negligible.

As seen in the figures, the xenon points measured in VTF-1 match relatively closely to the trends found in the P5 historical data despite operating with a mass flow rate of 5 mg/s compared to the mass flow rate range of 5.25–15 mg/s seen in the historical data. As expected, nitrogen has a consistently lower thrust, I_{sp} , and η_T than the argon and xenon propellants at a given discharge power, similar to the trends from existing literature [14,15]. Despite their similar mass and ionization cross sections, nitrogen is seen to have a much lower

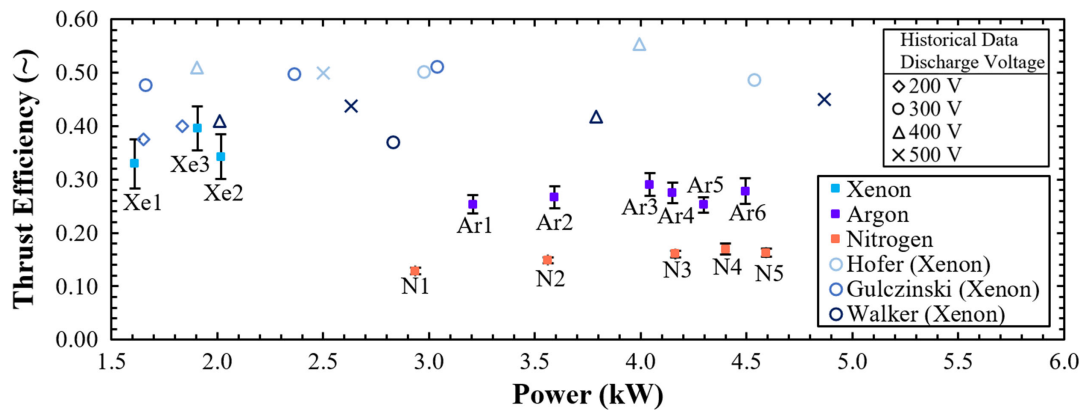


Fig. 7 P5 HET thrust efficiency as a function of discharge power on xenon, argon, and nitrogen. All historical data was run on xenon.

η_T (≈ 30 – 50%) across all setpoints compared to argon. Xenon has a much lower discharge power than nitrogen and argon (≈ 1 – 3 kW) because mass flow rate was matched across the setpoints. Since the particle mass of xenon is $4.7\times$ greater than nitrogen and $3.3\times$ greater than argon, this resulted in many fewer xenon particles compared to nitrogen and argon, which lowered the respective discharge current and overall power.

B. Global Efficiency Analysis

To decompose the thrust efficiency into the various efficiency terms, the first step is to see how well the new molecular efficiency model fits the experimental data compared to the atomic model. To do this, the η_T value calculated from the model (component calculated η_T) is compared to that calculated via direct thrust measurements (thrust calculated η_T) for all propellants, and the result is plotted in Fig. 8. In this figure, $\dot{m}_a = 5$ mg/s for all setpoints. The error bars in this figure are calculated using standard error propagation procedures from the base uncertainties summarized in Table 5. As seen in the figure, η_T calculated via both methods match reasonably well, within the error bars, across all discharge voltages and propellants. The nitrogen η_T calculated via the molecular efficiency model fits the thrust calculated η_T , and the atomic efficiency model fits the argon and xenon data, which serves as validation for the molecular efficiency model.

For both model types across all points and propellants except for the lowest V_d for xenon, the model slightly underpredicts η_T , with a maximum underprediction of 3.3%. This is similar to what Brown found from the atomic model, and attributed this underprediction to an overprediction of beam divergence [23]. A higher chamber pressure increases CEX collisions, artificially increases the beam divergence angle [47,66], and decreases the model calculated Ψ_b and η_T .

After model validation, η_T is decomposed into its components η_E , Φ_p , and Ψ_b , and each efficiency component is individually plotted

as a function of V_d as seen in Fig. 9. In this figure, $\dot{m}_a = 5$ mg/s for all setpoints. The error bars in this figure are calculated using standard error propagation procedures from the base uncertainties summarized in Table 5. Plotting the global efficiency terms allows for direct comparison between molecular and atomic efficiency terms. This plot, in conjunction with the energy flow diagrams presented in Sec. II, is used to see which energy sinks and efficiency terms have the largest impact on η_T across propellants.

First, from the Ψ_b term in Fig. 9, it is seen that Ψ_b is slightly higher for xenon but similar between argon and nitrogen; θ_d , the main contributor to Ψ_b , varies with CEX collision rate and position of the ionization and acceleration regions within the thruster [47]. Since the Ψ_b terms are similar between each of the propellants, there are either likely no major deviations between these components or the variations cancel each other out (e.g., higher CEX rate for xenon, but the ionization and acceleration regions are closer to the anode).

Next, from the η_E term in Fig. 9, since η_E is based on direct energy analysis, it is best to compare nitrogen and argon when distinguishing the unique characteristics between atomic and molecular propellants since they operated at approximately the same discharge power. Argon, compared to nitrogen, has a higher η_E across all discharge voltages and is also seen to diverge from nitrogen as V_d increases. One of the major components of η_E is η_b , and the molecular energy flow diagram illustrates that some of the energy sinks that correlate to η_b are rotational and vibrational excitation and dissociation, which are unique contributions for molecular propellants. These additional energy sinks likely contribute to the overall decrease in η_E for nitrogen compared to argon, and the plot suggests that these effects are amplified at higher V_d , which suggests that higher V_d influences increased dissociation and molecular excitation.

Finally, Φ_p from Fig. 9 exhibits the largest deviation between the atomic and molecular propellants and is the primary contributor for the low η_T seen in nitrogen. The decrease in Φ_p for nitrogen is due to

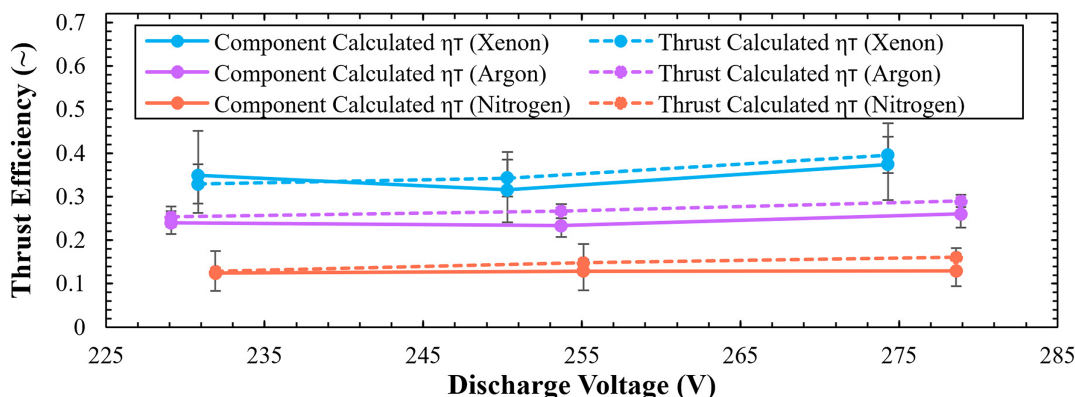


Fig. 8 Thrust efficiency calculated with direct thrust measurements and as a component of efficiency terms from plume diagnostics using the atomic (xenon and argon) and molecular (nitrogen) efficiency models.

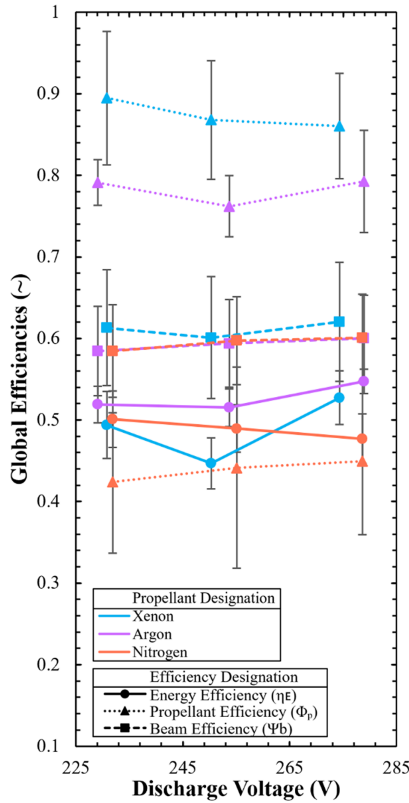


Fig. 9 Global efficiencies from atomic (xenon and argon) and molecular (nitrogen) efficiency models as a function of discharge voltage.

a much lower Φ_m (43%) compared to xenon (88%) and argon (78%), along with the larger effect Φ_s has on nitrogen (95%) compared to the effect Φ_q has on xenon and argon (both 99%). Some of the lower Φ_m for nitrogen is due to an $\approx 40\%$ smaller ionization cross section than argon, but it is also due to the effect of dissociation. This finding is discussed in further detail in the next section.

C. Nitrogen Species Efficiency

For increased fidelity into the nitrogen energy sinks, the species efficiencies for N and N_2 are calculated according to the molecular efficiency model and plotted in Fig. 10. In this figure, $\dot{m}_a = 5$ mg/s for all setpoints; η_{SP} is calculated using Eq. (10); $\eta_{n,V}$ is calculated using Eq. (11) and the definition of $\eta_{n,V}$ in Sec. II.C; and $\Phi_{m,n}$ is calculated using Eq. (12), the definition of $\Phi_{m,n}$ in Sec. II.C, and the ξ_n approximation outlined in Sec. III.E. The error bars in this figure are calculated using standard error propagation procedures from the base uncertainties summarized in Table 5.

Intuitively, one would think that producing N_2^+ ionic species would be much more efficient than producing N^+ species from nitrogen, since N_2^+ avoids the energy cost of dissociation, is a larger particle with a higher ionization cross section, and can ionize via a one-step direct ionization process as opposed to the two-step dissociation and ionization process seen with N^+ . For the voltage range from 230 to 275 V, Fig. 10 agrees with this intuition, as it shows that η_{SP} , which is a measure of relative species efficiency, for N_2^+ is higher than for N^+ . However, the gap between the η_{SP} values rapidly converges from a 21% difference to a 1.5% difference as V_d increases where η_{SP} for N_2^+ scales negatively with V_d , while η_{SP} for N^+ scales positively with V_d .

First, from the $\eta_{V,n}$ term, it is seen that $\eta_{V,N}$, perhaps surprisingly, is much higher (clearly outside the error bars) than η_{V,N_2} across all V_d . This indicates that N^+ and N_2^+ have different acceleration voltages and experience distinct ionization and acceleration regions, where the difference could occur either spatially or temporally. Gurciullo et al. measured acceleration voltages of ionic species of an air/xenon mixed propellant and also found that N^+ experienced a

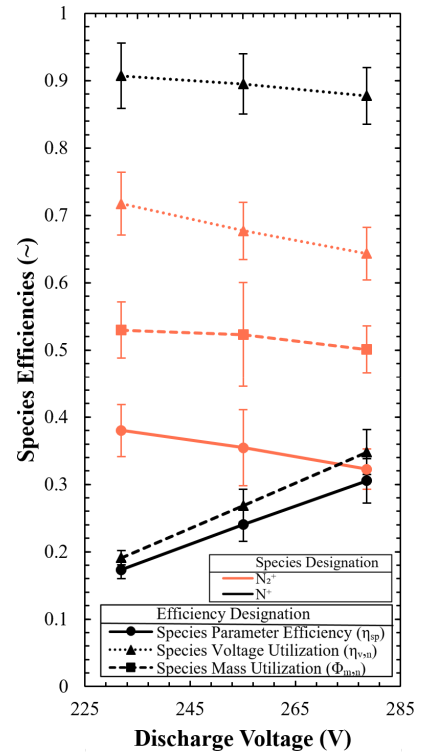


Fig. 10 Species efficiencies for nitrogen from the molecular efficiency model as a function of discharge voltage.

greater $V_{a,n}$ than N_2^+ [42]; however, the difference measured in that paper is not as apparent as is seen in Fig. 10. That may be due to the fact that the nitrogen propellant in this test is pure nitrogen as opposed to the air/xenon mixture used in Gurciullo et al., or the thruster is potentially running in a different operating mode than in Gurciullo et al. A better understanding of the ionization and acceleration process for nitrogen in a HET environment is needed since the difference in $\eta_{V,N}$ and η_{V,N_2} has a major impact on overall η_T and is different than what intuition suggests.

Next, from the $\Phi_{m,n}$ term, it is seen that Φ_{m,N_2} is much higher than $\Phi_{m,N}$ across all V_d . Φ_{m,N_2} is approximately where the predicted value would lie just due to differences in ionization cross section and mass using scaling laws between argon and nitrogen. $\Phi_{m,N}$, on the other hand, is much lower and decreases the global Φ_m for nitrogen. Ionization of atomic nitrogen is generally a two-step dissociation and ionization process [31,32], and atomic N is a relatively light particle with a high thermal velocity that will have a short residence time in the ionization region. Furthermore, the calculated dissociation reaction rate of nitrogen is similar to or greater than the molecular ionization reaction rate of nitrogen across a range of T_e using Eq. (19). This indicates that dissociation is a dominant mechanism throughout the discharge channel and there is a large supply of neutral N particles from the dissociation reaction. The high rate of dissociation, coupled with the relatively low probability of achieving both a dissociation and atomic ionization reaction before leaving a region of the discharge channel with sufficiently high electron energy, makes it difficult for N to achieve ample ionization. This causes many N particles to leave the discharge channel as neutrals instead of ionizing into N^+ , thus dropping Φ_m for nitrogen. However, the trends seen in Fig. 10 suggest that increasing V_d greatly mitigates this effect. As V_d increases, $\Phi_{m,N}$ and, as a result, $\eta_{SP,N}$ greatly increase, which leads to the conclusion that the N ionization rate is greatly enhanced at higher V_d . If this trend continues, N could surpass N_2 in terms of η_{SP} at higher V_d , which would indicate it could be more efficient to produce N^+ than N_2^+ at high V_d . These theories can be validated or rejected in the future by taking OES or TALIF measurements at the thruster exit plane to measure relative concentrations of neutral N particles.

The modified molecular efficiency model allows the ability to track and quantify the strength of the pertinent energy sinks present

for molecular propellants to influence optimized molecular propellant HET design. In general, to increase nitrogen η_T based on the presented data, an optimized molecular HET should focus on either increasing the voltage utilization for the N_2^+ species and limiting overall dissociation, or enhancing the dissociation rate and targeting increasing the mass utilization of the N^+ species, potentially by operating at a higher V_d . The best option to pursue is likely based on the primary power level in which the thruster will operate and the dominant processes at that power level.

V. Conclusions

This paper introduces an efficiency model that holds for molecular propellants and can be used to diagnose major energy sinks in molecular propellant HETs to inform more optimized molecular thruster design. The molecular efficiency model decomposes anode thrust efficiency into energy, propellant, and beam efficiency similar to existing atomic models and then further splits the efficiencies into global and species efficiencies. The global efficiencies are used to compare efficiencies between thrusters or types of propellants using a standard baseline, while species efficiencies are used to compare the efficiencies between various ionic species produced from a molecular propellant. This paper then maps the efficiencies to various energy sinks in an energy flow model to better understand the physical processes that cause degraded efficiency values for molecular propellants.

The authors apply the atomic and molecular efficiency models to experimental data from a 5 kW HET run on nitrogen, argon, and xenon. This data validates the molecular efficiency model and garners several key findings that describe the ionization process of nitrogen in a HET and grants insight into some of the prevalent molecular specific energy sinks that lead to the degraded nitrogen efficiency. First, this study finds that dissociation is a dominant nitrogen reaction mechanism, and this mechanism cannot be neglected in models and analyses specific to molecular propellant operation in a HET. Second, nitrogen is shown to experience a decreased energy efficiency compared to argon at similar discharge powers and voltages, likely due to the presence of molecular-specific energy sinks such as rotational and vibrational excitation and dissociation. Third, nitrogen exhibits a poor mass utilization of dissociated atomic nitrogen particles, which greatly decreases the relative propellant efficiency and mass utilization of nitrogen compared to argon and xenon propellants. Fourth, another major, perhaps unexpected, finding is that the N^+ voltage utilization is much higher than the N_2^+ voltage utilization, which indicates that N_2^+ and N^+ on average experience spatially or temporally distinct ionization and acceleration regions in a HET. Finally, with a discharge voltage from 230 to 275 V and a mass flow rate of 5.0 mg/s in the P5 HET, N_2^+ is seen to be the more efficient species to produce over N^+ . However, at the high V_d range, N^+ becomes almost as efficient to produce as N_2^+ and could potentially overtake N_2^+ efficiency if V_d were further increased. In this test the molecular efficiency model was applied to nitrogen, but it similarly can be applied to other molecular propellants and mixtures of propellants.

Following are some considerations and author recommendations when using this molecular efficiency model and analysis. The authors first recommend, if possible, to use OES or TALIF at the thruster exit plane to directly measure neutral dissociated particle concentrations and more accurately calculate the species fraction. Additionally, since energy is transferred between electrons and heavy molecules probabilistically via electron–neutral collisions, the authors also recommend producing a high-fidelity kinetic model of probable reaction mechanisms for the associated molecular propellant. This will grant insight into probable energy sinks and kinetic processes to base the molecular efficiency analysis.

Acknowledgments

This material is based upon work supported by the National Science Foundation Graduate Research Fellowship under Grant No. DGE-2039655. Any opinion, findings, and conclusions or

recommendations expressed in this material are those of the authors and do not necessarily reflect the views of the National Science Foundation.

References

- [1] Tirila, V., Demaire, A., and Ryan, C., “Review of Alternative Propellants in Hall Thrusters,” *Acta Astronautica*, Vol. 212, Nov. 2023, pp. 284–306.
<https://doi.org/10.1016/j.actaastro.2023.07.047>
- [2] Rovey, J. L., Lyne, C. T., Mundahl, A. J., Rasmont, N., Glascock, M. S., Wainwright, M. J., and Berg, S. P., “Review of Multimode Space Propulsion,” *Progress in Aerospace Sciences*, Vol. 118, Oct. 2020, Paper 100627.
<https://doi.org/10.1016/j.paerosci.2020.100627>
- [3] Koizumi, H., Inagaki, T., Kasagi, Y., Naoi, T., Hayashi, T., Funase, R., and Komurasaki, K., “Unified Propulsion System to Explore Near-Earth Asteroids by a 50 kg Spacecraft,” *28th Annual AIAA/USU Conference on Small Satellites*, Paper SSC14-VI-6, 2014.
- [4] Little, B., and Jugroot, M., “Bimodal Propulsion System for Small Spacecraft: Design, Fabrication, and Performance Characterization,” *Journal of Propulsion and Power*, Vol. 57, No. 4, 2020, pp. 707–719.
<https://doi.org/10.2514/1.A34555>
- [5] Schwertheim, A., Muir, C., Knoll, A., Ferreri, A., Sadler, J., Galdamez, C., and Staab, D., “Experimentally Demonstrating the Feasibility of Water as a Multimode Electric-Chemical Propellant,” *37th International Electric Propulsion Conference*, IEPC Paper 2022-426, 2022.
- [6] Tisaev, M., Ferrato, E., Giannetti, V., Pissoni, C., Baresi, N., Lucca Fabris, A., and Andreussi, T., “Air-Breathing Electric Propulsion: Flight Envelope Identification and Development of Control for Long-Term Orbital Stability,” *Acta Astronautica*, Vol. 191, Feb. 2022, pp. 374–393.
<https://doi.org/10.1016/j.actaastro.2021.11.011>
- [7] Crisp, N. H., Roberts, P. C. E., Livadiotti, S., Oiko, V. T. A., Edmondson, S., Haigh, S. J., Huyton, C., Sinpetru, L. A., Smith, K. L., Worral, S. D., et al., “The Benefits of Very Low Earth Orbit for Earth Observation Missions,” *Progress in Aerospace Sciences*, Vol. 117, Paper 100619, Aug. 2020.
<https://doi.org/10.1016/j.paerosci.2020.100619>
- [8] Zheng, P., Wu, J., Zhang, Y., and Wu, B., “A Comprehensive Review of Atmosphere-Breathing Electric Propulsion Systems,” *International Journal of Aerospace Engineering*, Vol. 2020, Oct. 2020, pp. 1–21.
<https://doi.org/10.1155/2020/8811847>
- [9] Singh, L. A., and Walker, M. L. R., “A Review of Research in Low Earth Orbit Propellant Collection,” *Progress in Aerospace Sciences*, Vol. 75, May 2015, pp. 15–25.
<https://doi.org/10.1016/j.paerosci.2015.03.001>
- [10] Andreussi, T., Ferrato, E., and Giannetti, V., “A Review of Air-Breathing Electric Propulsion: From Mission Studies to Technology Verification,” *Journal of Electric Propulsion*, Vol. 1, No. 31, 2022, pp. 1–31.
<https://doi.org/10.1007/s44205-022-00024-9>
- [11] Borrfor, A. N., Harding, D. J., Weissenrieder, J., Ciaralli, S., Hallock, A., and Brinck, T., “Aromatic Hydrocarbons as Molecular Propellants for Electric Propulsion Thrusters,” *Journal of Electric Propulsion*, Vol. 2, No. 24, 2023, pp. 2–24.
<https://doi.org/10.1007/s44205-023-00059-6>
- [12] Schwertheim, A., and Knoll, A., “Low Power Thrust Measurements of the Water Electrolysis Hall Effect Thruster,” *CEAS Space Journal*, Vol. 14, No. 1, March 2022, pp. 3–17.
<https://doi.org/10.1007/s12567-021-00350-y>
- [13] Rafalskiy, D., Martínez, J. M., Hahl, L., Zorzoli Rossi, E., Proynov, P., Boré, A., Baret, T., Poyet, A., Lafleur, T., Dudin, S., and Aanesland, A., “In-Orbit Demonstration of an Iodine Electric Propulsion System,” *Nature*, Vol. 599, No. 7885, Nov. 2021, pp. 411–415.
<https://doi.org/10.1038/s41586-021-04015-y>
- [14] Munro-O’Brien, T., and Ryan, C., “Performance of a Low Power Hall Effect Thruster with Several Gaseous Propellants,” *Acta Astronautica*, Vol. 206, May 2023, pp. 257–273.
<https://doi.org/10.1016/j.actaastro.2023.01.033>
- [15] Marchioni, F., and Cappelli, M., “Extended Channel Hall Thruster for Air-Breathing Electric Propulsion,” *Journal of Applied Physics*, Vol. 130, No. 5, 2021, Paper 053306.
<https://doi.org/10.1063/5.0048283>
- [16] Ferrato, E., Giannetti, V., Califano, F., and Andreussi, T., “Atmospheric Propellant Fed Hall Thruster Discharges: OD-Hybrid Model and Experimental Results,” *Plasma Sources Science and Technology*, Vol. 31, No. 7, 2022, Paper 233307.
<https://doi.org/10.1088/1361-6595/ac7904>

- [17] Cifali, G., Misuri, T., Rossetti, P., Andrenucci, M., Valentian, D., Feili, D., and Lotz, B., "Experimental Characterization of HET and RIT with Atmospheric Propellants," *32nd International Electric Propulsion Conference*, IEPC Paper 2011-224, 2011.
- [18] Hruby, V., Hohman, K., and Szabo, J., "Air Breathing Hall Effect Thruster Design Studies and Experiments," *37th International Electric Propulsion Conference*, IEPC Paper 2022-446, 2022.
- [19] Tejeda, J. M., and Knoll, A., "A Water Vapour Fuelled Hall Effect Thruster: Characterization and Comparison with Oxygen," *Acta Astronautica*, Vol. 211, Oct. 2023, pp. 702–715.
<https://doi.org/10.1016/j.actaastro.2023.06.046>
- [20] Shirasu, K., Kuwabara, H., Matsuura, M., Koizumi, H., Nakagawa, Y., Watanabe, H., Sekine, H., and Komurasaki, K., "Demonstration and Experimental Characteristics of a Water-Vapor Hall Thruster," *Journal of Electric Propulsion*, Vol. 2, No. 11, 2023, pp. 2–11.
<https://doi.org/10.1007/s44205-023-00047-w>
- [21] Hofer, R., and Gallimore, A. D., "High-Specific Impulse Hall Thrusters, Part 2: Efficiency Analysis," *Journal of Propulsion and Power*, Vol. 22, No. 4, 2006, pp. 732–740.
<https://doi.org/10.2514/1.15954>
- [22] Hofer, R. R., "Development and Characterization of High-Efficiency, High-Specific Impulse Xenon Hall Thrusters," Ph.D. Dissertation, Aerospace Engineering Dept., Univ. of Michigan, Ann Arbor, MI, 2004.
- [23] Brown, D. L., Larson, C. W., Beal, B. E., and Gallimore, A. D., "Methodology and Historical Perspective of a Hall Thruster Efficiency Analysis," *Journal of Propulsion and Power*, Vol. 25, No. 6, 2009, pp. 1163–1177.
<https://doi.org/10.2514/1.38092>
- [24] Brown, D. L., "Investigation of Low Discharge Voltage Hall Thruster Characteristics and Evaluation of Loss Mechanisms," Ph.D. Dissertation, Aerospace Engineering Dept., Univ. of Michigan, Ann Arbor, MI, 2009.
- [25] Dietz, P., Gartner, W., Koch, Q., Kohler, P. E., Teng, Y., Shreiner, P. R., Holste, K., and Klar, P. J., "Molecular Propellants for Ion Thrusters," *Plasma Sources Science and Technology*, Vol. 28, No. 8, 2019, p. 2019.
<https://doi.org/10.1088/1361-6595/ab2c6c>
- [26] Martinez, R. A., Dao, H., and Walker, M., "Power Deposition into the Discharge Channel of a Hall Effect Thruster," *Journal of Propulsion and Power*, Vol. 30, No. 1, 2014, pp. 209–220.
<https://doi.org/10.2514/1.B34897>
- [27] Mazouffre, S., Dannenmayer, K., and Blank, C., "Impact of Discharge Voltage on Wall-Losses in a Hall Thruster," *Physics of Plasmas*, Vol. 18, No. 6, 2011, Paper 064501.
<https://doi.org/10.1063/1.3592251>
- [28] Mikellides, I. G., Katz, I., Hofer, R. R., and Goebel, D. M., "Hall-Effect Thruster Simulations with 2-D Electron Transport and Hydrodynamic Ions," *31st International Electric Propulsion Conference*, IEPC Paper 2009-114, 2009.
- [29] Boeuf, J., "Tutorial: Physics and Modeling of Hall Thrusters," *Journal of Applied Physics*, Vol. 121, No. 1, 2017, Paper 011101.
<https://doi.org/10.1063/1.4972269>
- [30] Lide, D. R., "Ionization Energies of Gas-Phase Molecules," *Handbook of Chemistry and Physics*, 84th ed., CRC Press, Boca Raton, FL, 2004, pp. 181–198.
- [31] Wronski, Z., "Dissociation of Nitrogen in the Plasma-Cathode Interface of Glow Discharges," *Vacuum*, Vol. 78, No. 2, 2005, pp. 641–647.
<https://doi.org/10.1016/j.vacuum.2005.01.113>
- [32] Li, Z., Wu, E., Nie, L., Liu, D., and Lu, X., "Magnetic Field Stabilized Atmospheric Pressure Plasma Nitrogen Fixation: Effect of Electric Field and Gas Temperature," *Physics of Plasmas*, Vol. 30, No. 8, 2023, Paper 083502.
<https://doi.org/10.1063/5.0155713>
- [33] Hayashi, M., "Bibliography of Electron and Photon Cross Sections with Atoms and Molecules Published in the 20th Century—Argon," *National Institute for Fusion Science NIFS-DATA-72*, Jan. 2003.
- [34] Linstrom, P., "NIST Chemistry WebBook—SRD 69," *National Institute of Standards and Technology*, retrieved 22 Feb. 2024.
<https://doi.org/10.18434/T4D303>
- [35] Gaydon, A. G., and Penney, W. G., "The Dissociation Energies of CO, N₂, NO, and CN," *Proceedings of the Royal Society of London A*, Vol. 183, No. 995, 1945, pp. 374–388.
<https://doi.org/10.1098/rspa.1945.0009>
- [36] Dankanich, J., Walker, M., Swiatek, M., and Yim, J., "Recommended Practice for Pressure Measurement and Calculation of Effective Pumping Speed in Electric Propulsion Testing," *Journal of Propulsion and Power*, Vol. 33, No. 3, 2017, pp. 668–680.
<https://doi.org/10.2514/1.B35478>
- [37] Gulczynski, F. S., "Examination of the Structure and Evolution of Ion Energy Properties of a 5 kW Class Laboratory Hall Effect Thruster at Various Operational Conditions," Ph.D. Dissertation, Aerospace Engineering Dept., Univ. of Michigan, Ann Arbor, MI, 1999.
- [38] Haas, J., "Low-Perturbation Interrogation of the Internal and Near-Field Plasma Structure of a Hall Thruster Using a High-Speed Probe Positioning System," Ph.D. Dissertation, Aerospace Engineering Dept., Univ. of Michigan, Ann Arbor, MI, 2001.
- [39] Walker, M. L. R., "Effects of Facility Backpressure on the Performance Plume of a Hall Thruster," Ph.D. Dissertation, Aerospace Engineering Dept., Univ. of Michigan, Ann Arbor, MI, 2005.
- [40] Polk, J., Haag, T., King, S., Walker, M., Blakely, J., and Ziemer, J., "Recommended Practice for Thrust Measurement in Electric Propulsion Testing," *Journal of Propulsion and Power*, Vol. 33, No. 3, 2017, pp. 539–555.
<https://doi.org/10.2514/1.B35564>
- [41] Kim, S., and Gallimore, A. D., "Plume Study of a 1.35-kW SPT-100 Using an ExB Probe," *Journal of Spacecraft and Rockets*, Vol. 39, No. 6, 2002, pp. 904–909.
<https://doi.org/10.2514/2.3897>
- [42] Gurciullo, A., Fabris, A. L., and Cappelli, M. A., "Ion Plume Investigation of a Hall Effect Thruster Operating with Xe/N₂ and Xe/Air Mixtures," *Journal of Physics D: Applied Physics*, Vol. 52, No. 46, 2019, Paper 464003.
<https://doi.org/10.1088/1361-6463/ab36c5>
- [43] Huang, W., and Shastry, R., "Analysis of Wien Filter Spectra from Hall Thruster Plumes," *Review of Scientific Instruments*, Vol. 86, No. 7, 2015, Paper 073502.
<https://doi.org/10.1063/1.4923282>
- [44] Lobbia, R., and Beal, B., "Recommended Practice for Use of Langmuir Probes in Electric Propulsion Testing," *Journal of Propulsion and Power*, Vol. 33, No. 3, 2017, pp. 566–581.
<https://doi.org/10.2514/1.B35531>
- [45] Frieman, J. D., Brown, N. P., Liu, C. Y., Liu, T. M., Walker, M. L. R., Khayms, V., and King, D. Q., "Electrical Facility Effects on Faraday Probe Measurements," *Journal of Propulsion and Power: Technical Notes*, Vol. 34, No. 1, 2018, pp. 267–269.
<https://doi.org/10.2514/1.B36467>
- [46] Walker, M. L. R., Hofer, R. R., and Gallimore, A. D., "The Effects of Nude Faraday Probe Design and Vacuum Facility Backpressure on the Measured Ion Current Density Profile of Hall Thruster Plumes," *38th AIAA/ASME/SAE/ASEE Joint Propulsion Conference and Exhibit*, AIAA Paper 2002-4253, 2002.
- [47] Brown, D., Walker, M., Szabo, J., Huang, W., and Foster, J., "Recommended Practice for Use of Faraday Probes in Electric Propulsion Testing," *Journal of Propulsion and Power*, Vol. 33, No. 3, 2017, pp. 582–613.
<https://doi.org/10.2514/1.B35696>
- [48] Xu, K., "Ion Collimation and In-Channel Potential Shaping Using In-Channel Electrodes for Hall-Effect Thruster," Ph.D. Dissertation, Aerospace Engineering Dept., Georgia Inst. of Technology, Atlanta, GA, 2012.
- [49] Piragino, A., Faraji, F., Reza, M., Ferrato, E., Piraino, A., and Andreussi, T., "Background Pressure Effects on the Performance of a 20 kW Magnetically Shielded Hall Thruster Operating in Various Configurations," *Aerospace*, Vol. 8, No. 3, 2021, p. 69.
<https://doi.org/10.3390/aerospace8030069>
- [50] Walker, M. L. R., Victor, A. L., Hofer, R. R., and Gallimore, A. D., "Effect of Backpressure on Ion Current Density Measurements in Hall Thruster Plumes," *Journal of Propulsion and Power*, Vol. 21, No. 3, 2005, pp. 408–415.
<https://doi.org/10.2514/1.7713>
- [51] Randolph, T., Kim, V., Kaufman, H., Kozubsky, K., and Day, M., "Facility Effects on Stationary Plasma Thruster Testing," *23rd International Electric Propulsion Conference*, IEPC Paper 1993-93, 1993.
- [52] Reid, B. M., "The Influence of Neutral Flow Rate in the Operation of Hall Thrusters," Ph.D. Dissertation, Aerospace Engineering Dept., Univ. of Michigan, Ann Arbor, MI, 2009.
- [53] Azziz, Y., "Experimental and Theoretical Characterization of a Hall Thruster Plume," Ph.D. Dissertation, Dept. of Aeronautics and Astronautics, Massachusetts Inst. of Technology, Cambridge, MA, 2007.
- [54] Taylor, B. N., and Kuyatt, C. E., "Guidelines for Evaluating and Expressing the Uncertainty of NIST Measurement Results," NIST TN 1297, 1994.
- [55] Chapurin, O., Smolyakov, A. I., Hagelaar, G., and Raites, Y., "On the Mechanism of Ionization Oscillations in Hall Thrusters," *Journal of Applied Physics*, Vol. 129, No. 23, 2021.
<https://doi.org/10.1063/5.0049105>
- [56] Vojnović, M., Popović, M., Ristić, M. M., Vičić, M. D., and Poparić, G. B., "Rate Coefficients for Electron Impact Excitation of N₂," *Chemical Physics*, Vol. 463, Dec. 2015, pp. 38–46.
<https://doi.org/10.1016/j.chemphys.2015.09.014>

- [57] Hleli, A., Riahi, R., Teulet, P., Cressault, Y., and Ghalila, H., "Calculation of Electron-Impact Excitation and Ionization Cross Sections and Reaction Rate Coefficients for C, N and O Atoms," *Journal of Physics: Conference Series*, Vol. 1243, No. 1, 2019, Paper 012014. <https://doi.org/10.1088/1742-6596/1243/1/012014>
- [58] Itikawa, Y., "Cross Sections for Electron Collisions with Nitrogen Molecules," *Journal of Physical and Chemical Reference Data*, Vol. 35, No. 1, 2006, pp. 31–53. <https://doi.org/10.1063/1.1937426>
- [59] Cosby, P. C., "Electron-Impact Dissociation of Nitrogen," *Journal of Chemical Physics*, Vol. 98, No. 12, 1993, pp. 9544–9553. <https://doi.org/10.1063/1.464385>
- [60] Raites, Y., Smirnov, A., Staack, D., and Fisch, N. J., "Measurements of Secondary Electron Emission Effects in the Hall Thruster Discharge," *Physics of Plasmas*, Vol. 13, No. 1, 2006, Paper 014502. <https://doi.org/10.1063/1.2162809>
- [61] Haas, J., and Gallimore, A., "An Investigation of Internal Ion Number Density and Electron Temperature Profiles in a Laboratory-Model Hall Thruster," *36th AIAA/ASME/SAE/ASEE Joint Propulsion Conference*, AIAA Paper 2000-3422, 2000. <https://doi.org/10.2514/6.2000-3422>
- [62] Siasko, A., Golubovskii, Yu, Pavlov, S., Dzlieva, E., Novikov, L., Golubev, M., and Karasev, V., "About the Measurement of Electric Field and Electron Temperature by the Spectroscopic Method in a Gas Mixture," *Physics of Plasmas*, Vol. 30, No. 3, 2023, Paper 033701. <https://doi.org/10.1063/5.0135329>
- [63] Levaton, J., Klein, A. N., and Amorim, J., "Neutral and Excited Molecules and Atoms Densities in the Positive Column of Flowing N₂ DC Discharges," *Brazilian Journal of Physics*, Vol. 51, No. 1, Oct. 2020, pp. 75–81. <https://doi.org/10.1007/s13538-020-00809-z>
- [64] Kanazawa, S., Mizeraczyk, J., Nakatani, T., Kuno, A., Furuki, T., Tachibana, K., Ichiki, R., and Kocik, M., "Implementation of a Single-Shot LIF Technique for 2-D Imaging of Metastable Nitrogen Molecules in a Discharge Afterglow at Sub-Atmospheric Pressures," *Measurement*, Vol. 196, June 2022, Paper 111262. <https://doi.org/10.1016/j.measurement.2022.111262>
- [65] Cohen, L., and Hanson, R., "Emission and Laser-Induced Fluorescence Measurements in a Supersonic Jet of Plasma-Heated Nitrogen," *Journal of Physics D: Applied Physics*, Vol. 25, No. 3, 1992, pp. 339–351. <https://doi.org/10.1088/0022-3727/25/3/001>
- [66] Mundy, D. H., Fearn, D. G., and Bond, R. A., "The Influence of Charge-Exchange Ions on the Beam Divergence of an Ion Thruster," *27th International Electric Propulsion Conference*, IEPC Paper 2001-111, 2001.

J. Blandino
Associate Editor